Title

Verification of long wavelength electromagnetic modes with a gyrokinetic-fluid hybrid model in the XGC code

Journal
Physics of Plasmas, 24(5)

ISSN
1070-664X

Authors
Hager, Robert
Lang, Jianying
Chang, CS
et al.

Publication Date
2017-05-01

DOI
10.1063/1.4983320

Peer reviewed

Verification of long wavelength electromagnetic modes with a gyrokinetic-fluid hybrid model in the XGC code

Robert Hager, Jianying Lang, C. S. Chang, S. Ku, Y. Chen, S. E. Parker, and M. F. Adams

Citation: Physics of Plasmas **24**, 054508 (2017); doi: 10.1063/1.4983320
View online: https://doi.org/10.1063/1.4983320
View Table of Contents: http://aip.scitation.org/toc/php/24/5
Published by the American Institute of Physics

Verification of long wavelength electromagnetic modes with a gyrokinetic-fluid hybrid model in the XGC code

Robert Hager,[1,a)] Jianying Lang,[2] C. S. Chang,[1] S. Ku,[1] Y. Chen,[3] S. E. Parker,[3] and M. F. Adams[4]
[1]*Princeton Plasma Physics Laboratory, P.O. Box 451, Princeton, New Jersey 08543, USA*
[2]*Intel Corporation, 2200 Mission College Blvd., Santa Clara, California 95054, USA*
[3]*University of Colorado, 2000 Colorado Avenue, Boulder, Colorado 80309, USA*
[4]*Lawrence Berkeley National Laboratory, 1 Cyclotron Road, Berkeley, California 94720, USA*

(Received 11 February 2017; accepted 25 April 2017; published online 24 May 2017)

As an alternative option to kinetic electrons, the gyrokinetic total-f particle-in-cell (PIC) code XGC1 has been extended to the MHD/fluid type electromagnetic regime by combining gyrokinetic PIC ions with massless drift-fluid electrons analogous to Chen and Parker [Phys. Plasmas **8**, 441 (2001)]. Two representative long wavelength modes, shear Alfvén waves and resistive tearing modes, are verified in cylindrical and toroidal magnetic field geometries. *Published by AIP Publishing.*
[http://dx.doi.org/10.1063/1.4983320]

This article describes the verification of two important MHD/fluid type, long-wavelength, electromagnetic modes after the addition of an optional kinetic-fluid hybrid model to the gyrokinetic particle-in-cell (PIC) code XGC1.[1] This work complements—as a more economical alternative—the fully implicit, fully kinetic electromagnetic formulation, that is also being developed for XGC1.[2]

The importance of MHD/fluid type electromagnetic modes in magnetically confined fusion devices, which operate regularly at moderate to high $\beta = 2\mu_0 P/B^2$ (the ratio of thermodynamic to magnetic pressure), is widely recognized. Examples are neoclassical tearing modes,[3] sawtooth oscillations,[4] and edge localized modes (ELMs).[5] Gyrokinetic electromagnetic codes such as GYRO,[6,7] GS2,[8] GENE,[9] and GEM[10–12] have been available with increasing physics capability for more than a decade and have also been used to study those modes. However, their application in long wavelength MHD/fluid type instabilities has been difficult, especially for PIC codes, due to the so called "cancellation problem."[13,14] Recently, several methods were developed to overcome the cancellation problem with kinetic electrons for particle codes: the control variate method,[15] a special splitting of the vector potential[16,17] (used, e.g., by the EUTERPE code), and the split-weight method[12,18] (used in GEM, and being further developed in GTS[19]). The XGC1 code[1] recently demonstrated fully kinetic electromagnetic capability without the cancellation problem[2] using a fully implicit electromagnetic scheme based on the work by Chen and Chacón.[20–22] These methods are computationally expensive for long wave length MHD/fluid type modes even without the cancellation problem. The cheapest way to study these modes is to use fluid electrons instead of electron particles.

Long wavelength electromagnetic physics in the global edge region has so far been studied with fluid and MHD codes (some of them with *ad hoc* kinetic ion effect) such as BOUT++,[23,24] M3D,[25,26] M3D-C1,[27,28] and JOREK,[29,30] which neglect important effects that drive the plasma to a non-thermal equilibrium. Since kinetic ion effects on fluid/MHD modes as well as microturbulence are expected to be important in the plasma edge region, e.g., for the physics of edge localized modes (ELMs), kinetic ballooning modes (KBM) and others, the fluid and MHD approach was improved by coupling gyrokinetic ions to the massless electron fluid hybrid model utilized in the GEM code.[10,11] Although the fluid treatment of the electrons drops some important effects such as the trapped electron mode (TEM), it is still attractive because its implementation is rather straightforward without the cancellation issue, low $k_\perp$ fluid/MHD modes are important for ELM activity, and it is economical with computing time.

The fluid-kinetic hybrid version of the XGC1 code used in this report combines gyrokinetic ions in the δf formalism[1] (which, if done correctly, can be made identical to the total-f formalism[31]) with massless drift-fluid electrons.[11,32] The electron density continuity equation is given by

$$\begin{aligned}\frac{\partial \delta n_e}{\partial t} = &-n_0(\boldsymbol{B} + \delta\boldsymbol{B}_\perp)\cdot\nabla\left(\frac{\nabla_\perp^2 A_\parallel}{e\mu_0 n_0 B} + \frac{u_{\parallel,i}}{B}\right)\\ &+\delta\boldsymbol{B}_\perp\cdot\nabla\frac{j_0}{eB} - \boldsymbol{v}_E\cdot\nabla(n_0+\delta n_e)\\ &-\frac{2n_0}{B^3}(\boldsymbol{B}\times\nabla B)\cdot\nabla\phi\\ &+\frac{2}{eB^3}(\boldsymbol{B}\times\nabla B)\cdot\nabla\delta P_e,\end{aligned} \tag{1}$$

where $\boldsymbol{B}$ is the axisymmetric background magnetic field, $\delta\boldsymbol{B}_\perp = \nabla A_\parallel \times \hat{\boldsymbol{b}}$ is the perturbed magnetic field, $\hat{\boldsymbol{b}} = \boldsymbol{B}/B$, and $A_\parallel$ is the component of the perturbed vector potential along the background magnetic field, μ_0 is the vacuum permeability, $u_{\parallel,i} = \int d^3v v_\parallel \delta f_i/n_0$ is the parallel ion fluid flow, δf_i is the perturbed ion guiding center distribution function, $n_e = n_0 + \delta n_e$ is the electron density, $j_0 = \hat{\boldsymbol{b}}\cdot\nabla\times(\boldsymbol{B}/\mu_0)$ is the equilibrium current density, $\delta P_e = e\delta n_e T_{0,e}$ is the

a)Electronic mail: rhager@pppl.gov

perturbed iso-thermal electron pressure, and $\boldsymbol{v}_E = \frac{1}{B}\hat{\boldsymbol{b}} \times \nabla\phi$ is the $\boldsymbol{E} \times \boldsymbol{B}$ drift. We also used the relation $u_{\parallel,e} = \left(\nabla_\perp^2 A_\parallel\right)/(e\mu_0 n_0) + u_{\parallel,i}$. The time evolution of the perturbed vector potential is given by the definition of the electric field and Ohm's law

$$\frac{\partial A_\parallel}{\partial t} = -\hat{\boldsymbol{b}} \cdot \nabla\phi - E_\parallel, \tag{2}$$

$$E_\parallel = -\frac{\tilde{\boldsymbol{b}} \cdot \nabla}{en_0}\delta P_e - \frac{\delta \boldsymbol{B}_\perp}{en_0 B} \cdot \nabla(P_{0,e} - en_0\phi) + \eta_e j_\parallel. \tag{3}$$

Here, $\tilde{\boldsymbol{b}} = \hat{\boldsymbol{b}} + \delta\boldsymbol{B}_\perp/B$, $P_{0,e} = en_0 T_{0,e}$ is the background electron pressure, and $j_\parallel = en_0(u_{\parallel,i} - u_{\parallel,e})$. Finally, the gyrokinetic Poisson equation in the long wave length limit is

$$-\nabla \cdot \frac{\epsilon_0 \chi}{e}\nabla\phi = \delta n_i - \delta n_e, \tag{4}$$

where $\chi = \left(\rho_i/\lambda_{D,i}\right)^2 = (c/v_A)^2$ is the ion electric susceptibility, ρ_i is the ion gyro radius, $\lambda_{D,i}$ is the ion Debye length, and $v_A = B/(\mu_0 m_i n_0)^{1/2}$ is the Alfvén speed. The ion density is $\delta n_i = \int d^3v \langle \delta f_i \rangle_\rho$, where $\langle \ldots \rangle_\rho$ indicates gyro-averaging. The massless electron approximation is valid in the limit $v_A/v_{t,e} \to 0$ or $\beta_e m_i/m_e \gg 1$, where $\beta_e = 2\mu_0 P_e/B^2$.

The fluid equations are implemented by using a mixed finite-difference (FD) finite-element (FE) method. Terms of the form $\boldsymbol{a} \cdot \nabla$ and $\hat{\boldsymbol{b}} \cdot \nabla$ use a second order FD derivative. Parallel derivatives are set up by field-line tracing and exploiting the field-following property of the XGC meshes.[33,34] The Poisson equation and the Laplacian $\nabla_\perp^2$ retain only derivatives with respect to R and Z and are evaluated with linear finite elements on a planar triangular mesh.

In the δf formalism, the nonlinear terms in the electron fluid equations, e.g., $\boldsymbol{v}_E \cdot \nabla\delta n_e$, are a potential complication compared to the particle weight evolution equation,[1] which is formally linear with the non-linearity entering through the perturbed particle orbits. Based on preliminary nonlinear studies of KBM turbulence, we expect that this will not cause numerical problems. However, in some cases, numerical problems might arise and require adjustments to the implementation of the nonlinear terms, e.g., by casting the nonlinear terms in the electron continuity equation in a conservative form as in the GEM code.

Both explicit and implicit time integrators have been implemented. A second order Runge–Kutta (RK2) method has been utilized for the time integration of the combined particle–fluid system for many of the results discussed in this work. In the first step, $\delta n_e(t + \Delta t/2)$ and $A_\parallel(t + \Delta t/2)$ are evaluated using, $\phi(t)$, $\delta n_i(t)$ and $u_{\parallel,i}(t)$. Then the particles are pushed for a half time step to evaluate $\delta n_i(t + \Delta t/2)$ and $u_{\parallel,i}(t + \Delta t/2)$. In the second step, we evaluate $\phi(t + \Delta t/2)$ and then push the particles for a full time step to obtain $\phi(t + \Delta t)$, $\delta n_i(t + \Delta t)$ and $u_{\parallel,i}(t + \Delta t)$.

Implicit time stepping methods have been implemented using the PETSc TS framework[35–37] to overcome the restrictions in the time step of explicit methods. The particle terms δn_i and $u_{\parallel,i}$ are treated as non-linear contributions to the system of electron fluid equations and are fully integrated into PETSc's nonlinear solver residual, but only the electron fluid terms are included in the Jacobian. The Newton method is used to solve the non-linear equations, which requires one particle push per evaluation of the residual.

For the verification of shear Alfvén wave physics, we use a minimal system that supports this mode: linearized versions of equations (1)–(3) with the closure $E_\parallel = \eta_e j_\parallel$. In addition, we neglect the terms related to the curvature and ∇B drift in Eq. (1). It is straightforward to prove in cylindrical geometry that the dispersion relation of the resulting reduced system yields $\omega = [v_A 2k_\parallel^2 - 4\left(\eta_e/(2\mu_0)\right)^4 k_\perp^4]^{1/2} + i\eta_e/(2\mu_0)k_\perp^2$. The first verification test of the shear Alfvén dispersion relation was conducted in cylindrical geometry with concentric, circular flux-surfaces with minor radius $a = 1$, constant safety factor $q = 3$, $\beta_e = 1.5 \times 10^{-2}$, and $\eta_e = 10^{-6}\,\Omega\,\mathrm{m}$. The simulation was initialized with a global perturbation of $A_\parallel$ centered around $r/a = 0.67$ containing toroidal mode numbers $n = 1\ldots4$ and poloidal mode numbers $m = 0\ldots4$. With this large scale variation in the radial and poloidal direction, the low resistivity does not influence the real frequency much but still serves as a check for the resistive dissipation of the reduced shear Alfvén wave system (with $k_\perp \sim 1/a$). The time step for this simulation was $\Delta t = 1.36 \times 10^{-8}\,\mathrm{s} \approx 10^{-2}\tau_A$, where $\tau_A = R_0/v_A$. The total duration of the simulation is $1.36 \times 10^{-3}\,\mathrm{s} \approx 1000\tau_A$.

Figure 1 shows the shear Alfvén spectrum obtained from this simulation. The parallel wave number was determined as $k_\parallel = \hat{\boldsymbol{b}} \cdot \boldsymbol{k} = (B_P/B)k_\theta + (B_T/B)k_\varphi$. The mode frequency is the median of the intensity for each value of $k_\parallel$ and the error bars indicate the decay length of the mode intensity around its median. The increasing width of the error bars at $k_\parallel > 0.5$ indicates decreasing overall intensity due to the low toroidal and poloidal mode numbers used to initialize the simulation. The steps in the frequency spectrum are an artifact of the interpolation of the intensity from (k_θ, k_φ) space to a common $k_\parallel$ scale.

Similar tests in toroidal geometry have been performed in a slightly modified version of the standard cyclone geometry, with $R_0 = 1.7$, $a/R_0 = 0.358$, $B_0 = 1.9$, constant $q = 2$,

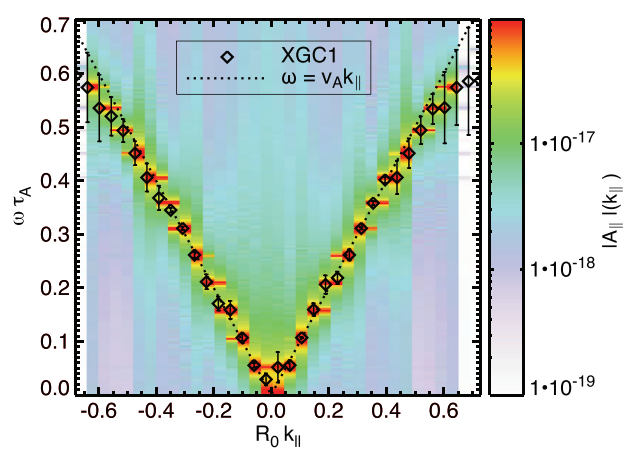

FIG. 1. The shear Alfvén wave spectrum in cylindrical geometry with concentric circular flux-surfaces. The density plot indicates the mode intensity, the diamonds indicate the median of the intensity at each $k_\parallel$, and the error bars indicate the decay length of the intensity around the median. The steps in the median frequency are an artifact of the interpolation of the intensity from (k_θ, k_φ) space to a common $k_\parallel$ scale.

and $T_0 = 2$ keV. The density is varied between $1.875 \times 10^{19}\,\mathrm{m}^{-3}$ and $6 \times 10^{20}\,\mathrm{m}^{-3}$ to achieve values of β_e between 0.4% and 13.4%. The time step is $\Delta t \approx 5 \times 10^{-2}\tau_A$ and the total simulation time is $\approx 40\tau_A$. The simulation is initialized with an $n = 4$, $m = 4\ldots12$ perturbation of $A_\parallel$. Figure 2 shows the frequency spectrum of the $n = 4$ Alfvén wave for the poloidal wave numbers $m = 6\ldots10$. The numerical frequencies agree very well with the (approximate) analytical result $\omega \propto (2\pi/L_\parallel)(n - m/q)v_A$, where $L_\parallel$ is the parallel connection length for one poloidal circuit. The deviations are caused by the variation of the field line pitch along magnetic field lines. We find that $\omega\tau_A$ is independent of β_e as expected because only the density n_0 was varied in this test.

Since the kinetic-fluid hybrid approach is especially useful for the simulation of low-n tearing modes, we benchmarked the $(m, n) = (2, 1)$ tearing mode in cylindrical and toroidal geometry against the GEM code[32] and M3D-K,[38] respectively. We did not consider the effect of kinetic ions in this benchmark. The only term added to the electron fluid equations compared to the terms kept in the shear Alfvén case is the kink drive $\delta\boldsymbol{B}_\perp \cdot \nabla\left[j_0/(eB)\right]$ in Eq. (1) to be consistent with GEM's eigenvalue solver.[32]

For the benchmark against the GEM code, we use the case described in Ref. 32: concentric, circular flux-surfaces in cylindrical geometry, $R_0 = 1.7$ m, $a = 0.425$ m ($R_0/a = 4$), $B_0 = 1.906$ T, $q = 1.5[1 + (r/a)^2]$, $Z = 1$, $m_i/m_p = 2.5$, and constant density $n_0 = 3.886 \times 10^{20}\,\mathrm{m}^{-3}$. Since the electron fluid equations used for this benchmark have no temperature dependence, we can use a constant temperature profile $T_{0,e} = 45.63$ eV, which yields the same on-axis β_e of 4×10^{-3} and relative domain size $a/\rho_i \approx 740$ as in Ref. 32. The resonant surface for the (2, 1) tearing mode is at $(r/a)_c \approx 0.577$ corresponding to the normalized poloidal magnetic flux $\psi_{N,c} = 0.411$. In order to be able to resolve the resonance layer of the (2, 1) tearing mode also at low resistivity, the radial resolution of our computational mesh varies between 0.5 mm around the resonant surface to a maximum of 8 mm far from the resonant surface. The relationship between the normalized resistivity η_N and growth rate γ_N used in Ref. 32 and the corresponding values η_e and γ in SI-units are $\eta_N = (en_0/B_0)\eta_e$ and $\gamma_N = m_p/(eB_0)\gamma$, where m_p is the proton mass. The results of a resistivity scan of the growth rate of the (2, 1) tearing mode in this geometry are shown in Fig. 3. The growth rates evaluated with XGC1 show excellent agreement with the growth rates computed with GEM's eigenvalue solver that uses the MHD approximation for the ion polarization density (Fig. 3 in Ref. 32). We did not include an XGC1 data point for $\eta_N = 10^{-7}$ because of the very strict resolution requirements of about 2.5×10^{-4} m or less for this low resistivity. Using the Crank–Nicolson method, the implicit time integrator could speed up these simulations by a factor of more than 10. For $\eta_N = 10^{-6}$ a time step of $\Delta t = 2.7\tau_A$ could be used.

For the benchmark against M3D-K in toroidal geometry, we use a Grad–Shafranov equilibrium generated with the FLOW code[39] with a fixed circular boundary, $R_0 = 5.76$ m, $a = 1$ m, $B_0 = 1$ T, $q = 1.5 + 2\psi_N^2$, $m_i/m_p = 2.5$, and constant $n_0 = 10^{20}\,\mathrm{m}^{-3}$ and $T_{0,e} = 100$ eV, so that $\beta_e = 4 \times 10^{-3}$ and $\beta_e m_i/m_e = 18.4$. The resonant surface of the (2, 1) tearing mode is located at $\psi_N = 0.5$. The radial resolution of the computational mesh is 1.5 mm between approximately $\psi_N = 0.4$ and $\psi_N = 0.6$ and up to 1.2 cm away from the tearing layer. For the normalized resistivity of $\eta_{M3D} = 10^{-4}$ used in Ref. 38 and the corresponding normalization relations, we obtain a resistivity in SI units of $\eta_e = \mu_0(a^2/\tau_A)\eta_{M3D} = 3.01 \times 10^{-4}$. The XGC1 growth rate calculation used a time

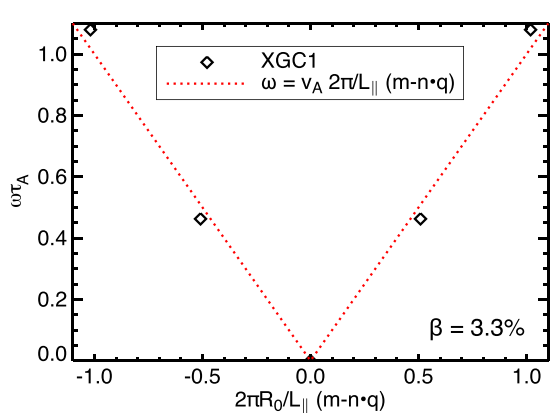

FIG. 2. Poloidal mode number scan ($m = 6\ldots10$) of the $n = 4$ shear Alfvén wave in a toroidal cyclone-like geometry for $\beta_e = 3.3 \times 10^{-3}$. The dotted line is the analytical mode frequency in cylindrical geometry.

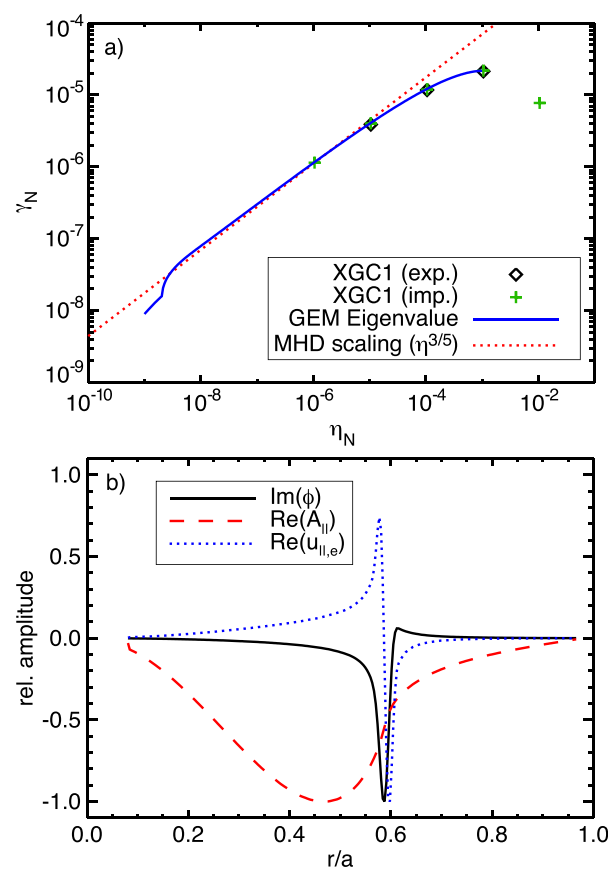

FIG. 3. (a) Growth rate of the (2, 1) tearing mode in cylindrical geometry. The solid line shows the result of GEM's tearing mode eigenvalue solver in the MHD approximation for the ion polarization density (see Ref. 32). The results from the implicit and explicit time integrator agree very well. (b) Mode structure of the $m = 2$ mode with $\eta_N = 10^{-5}$. The amplitude of each quantity is normalized to its respective maximum. The mode structure is similar to Fig. 8 in Ref. 32, although the tearing layer is shifted to a slightly higher r/a.

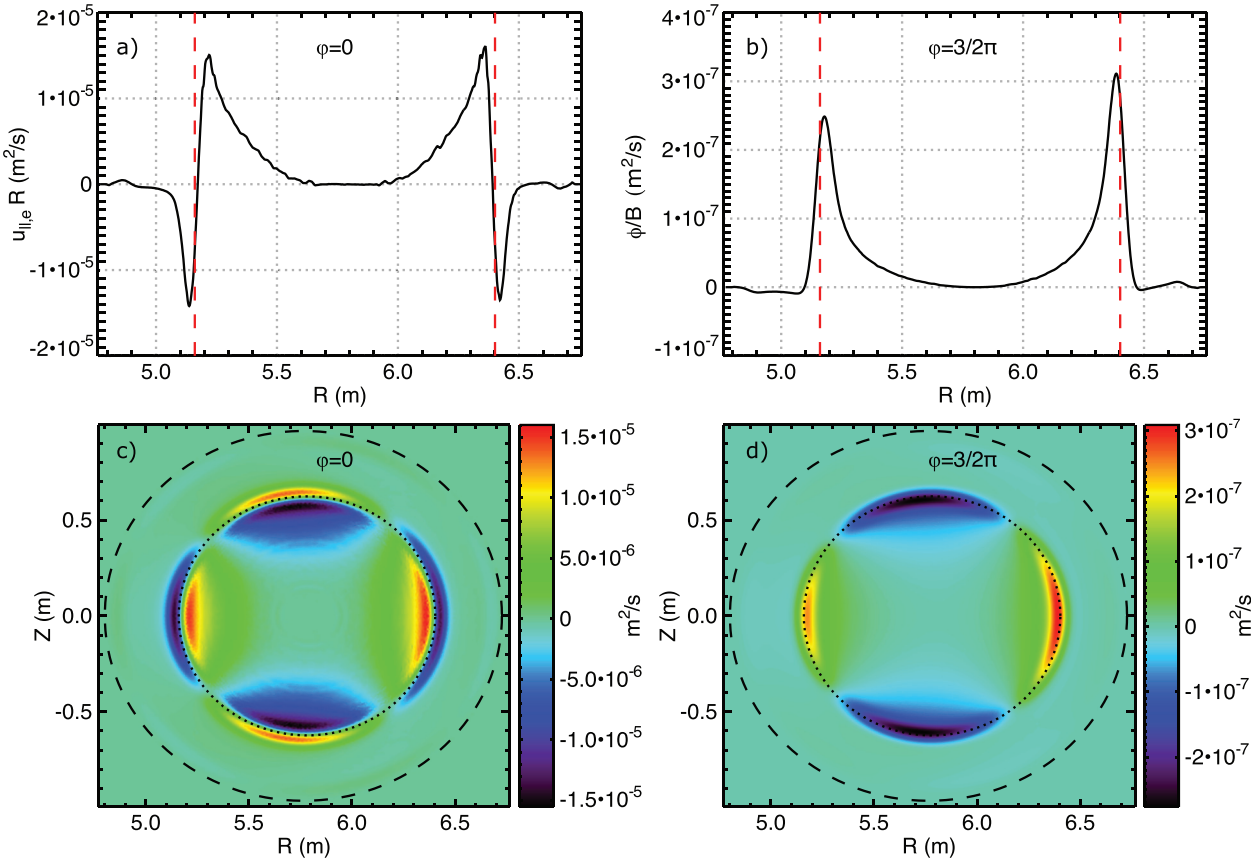

FIG. 4. Mode structure of the (2, 1) tearing mode in toroidal geometry, which compares well to Fig. 1 in Ref. 38. (a) $Ru_{\|,e}$ (equivalent to the perturbed current) at $\varphi = 0$, and (b) ϕ/B (velocity stream function) at $\varphi = 3\pi/2$ plotted along the midplane. The dashed lines indicate the location of the $\psi_N = 0.5$ surface. (c) $Ru_{\|,e}$ at $\varphi = 0$, and (d) ϕ/B at $\varphi = 3\pi/2$ in the (R, Z) plane. The dotted circle is the $\psi_N = 0.5$ surface.

step of $\Delta t = 7 \times 10^{-3}\tau_A$ and ran for a total time of approximately $350\,\tau_A$. Figures 4(a)–4(d) show the mode structure of the growing (2, 1) mode, which exhibits the usual tearing structure. For comparison with Ref. 38, we use reduced MHD quantities, the perturbed current $Ru_{\|,e}$, and the velocity stream function ϕ/B. The growth rate we obtain from the XGC1 calculation is $\gamma = 1.12 \times 10^{-2}\tau_A^{-1}$ and compares well to Ref. 38.

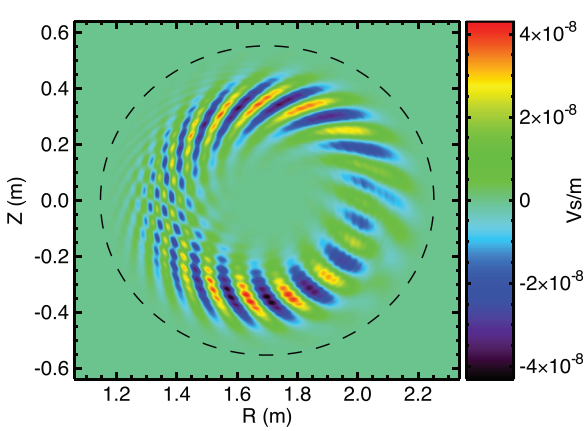

FIG. 5. Vector potential $A_\|$ obtained for the $n = 10$ mode after 65.7 τ_A in a linear XGC simulation in cyclone geometry with hydrogen ions, $R_0 = 1.7$ m, $a/R_0 = 0.358$, $B_0 = 1.9$ T, $q = 0.854 + 2.184(r/a)^2$, $T_i = T_e = 1$ keV, $\beta_e = 4.4\%$, $R_0/L_n = 2.22$, and $R_0/L_{T_i} = R_0/L_{T_e} = 10$.

The relative difference between the XGC1 and the M3D-K result is 6%.

Verification of linear and nonlinear intermediate wavelength drift-Alfvén modes such as ion temperature gradient-driven modes and kinetic ballooning modes (KBMs) will be presented in a future paper. In order to demonstrate the coupling of the gyrokinetic ion particles to the electron fluid equations, we give one example of linear growth of KBM modes in cyclone geometry with hydrogen ions, $R_0 = 1.7$ m, $a/R_0 = 0.358$, $B_0 = 1.9$ T, $q = 0.854 + 2.184(r/a)^2$, $T_i = T_e = 1$ keV, $\beta_e = 4.4\%$, $R_0/L_n = 2.22$ and $R_0/L_{T_i} = R_0/L_{T_e} = 10$. Figure 5 shows the final mode structure of the $n = 10$ mode of $A_\|$. The frequency and growth rate obtained in this case are $\omega = 2.0\,c_s/R_0$ and $\gamma = 0.69\,c_s/L_n$.

In order to add gyrokinetic ion effects to electromagnetic fluid/MHD instabilities, the gyrokinetic edge turbulence code XGC1 has been modified by replacing the kinetic electrons by massless drift-fluid electrons.[10,11] Explicit and implicit time integration methods have been implemented and tested. We verified shear Alfvén wave physics against the analytical solution and benchmarked the massless fluid model for resistive tearing modes against the codes GEM and M3D-K. The hybrid model in XGC will be further developed into a total-f code with the aim of studying the onset of edge localized modes across the magnetic separatrix surface. Verification of the kinetic version of peeling-ballooning

modes, and kinetic ballooning modes will be reported in a subsequent paper.

The authors would like to thank Guoyong Fu, Stephen Abbott, Peter Porazik, and Eduardo D'Azevedo for their support and fruitful discussions. Support for this work was provided through the Scientific Discovery through Advanced Computing (SciDAC) program funded by the U.S. Department of Energy Office of Advanced Scientific Computing Research and the Office of Fusion Energy Sciences. Notice: This manuscript has been authored by Princeton University under Contract No. DE-AC02-09CH11466 with the U.S. Department of Energy. The publisher, by accepting the article for publication, acknowledges that the United States Government retains a non-exclusive, paid-up, irrevocable, and world-wide license to publish or reproduce the published form of this manuscript, or allow others to do so, for the United States Government purposes.

[1]S. Ku, C. Chang, and P. Diamond, Nucl. Fusion **49**, 115021 (2009).
[2]S.-H. Ku, R. Hager, C. Chang, L. Chacón, and G. Chen, B. Am. Phys. Soc. **61**, GP10.00112 (2016).
[3]J. W. Connor, S. C. Cowley, R. J. Hastie, T. C. Hender, A. Hood, and T. J. Martin, Phys. Fluids **31**, 577 (1988).
[4]S. von Goeler, W. Stodiek, and N. Sauthoff, Phys. Rev. Lett. **33**, 1201 (1974).
[5]G. T. A. Huysmans, Plasma Phys. Controlled Fusion **47**, B165 (2005).
[6]J. Candy and R. E. Waltz, J. Comput. Phys. **186**, 545 (2003).
[7]J. Candy, Phys. Plasmas **12**, 072307 (2005).
[8]M. Kotschenreuther, G. Rewoldt, and W. Tang, Comput. Phys. Commun. **88**, 128 (1995).
[9]M. J. Pueschel, M. Kammerer, and F. Jenko, Phys. Plasmas **15**, 102310 (2008).
[10]S. E. Parker, Y. Chen, and C. C. Kim, Comput. Phys. Commun. **127**, 59 (2000).
[11]Y. Chen and S. Parker, Phys. Plasmas **8**, 441 (2001).
[12]Y. Chen and S. E. Parker, J. Comput. Phys. **189**, 463 (2003).
[13]J. C. Cummings, "Gyrokinetic simulation of finite-beta and self-generated sheared-flow effects on pressure-gradient-driven instabilities," Ph.D. thesis (Princeton University, 1995).
[14]A. Mishchenko, R. Hatzky, and A. Könies, Phys. Plasmas **11**, 5480 (2004).
[15]R. Hatzky, A. Knies, and A. Mishchenko, J. Comput. Phys. **225**, 568 (2007).
[16]A. Mishchenko, M. Cole, R. Kleiber, and A. Knies, Phys. Plasmas **21**, 052113 (2014).
[17]A. Mishchenko, A. Knies, R. Kleiber, and M. Cole, Phys. Plasmas **21**, 092110 (2014).
[18]W. W. Lee, J. L. V. Lewandowski, T. S. Hahm, and Z. Lin, Phys. Plasmas **8**, 4435 (2001).
[19]E. Startsev, W.-L. Lee, W. Wang, and Z. Lu, B. Am. Phys. Soc. **61**, BM9.00002 (2016).
[20]G. Chen and L. Chacón, Comput. Phys. Commun. **185**, 2391 (2014).
[21]G. Chen and L. Chacón, Comput. Phys. Commun. **197**, 73 (2015).
[22]L. Chacón and G. Chen, J. Comput. Phys. **316**, 578 (2016).
[23]B. Dudson, M. Umansky, X. Xu, P. Snyder, and H. Wilson, Comput. Phys. Commun. **180**, 1467 (2009).
[24]Z. X. Liu, X. Q. Xu, X. Gao, T. Y. Xia, I. Joseph, W. H. Meyer, S. C. Liu, G. S. Xu, L. M. Shao, S. Y. Ding, G. Q. Li, and J. G. Li, Phys. Plasmas **21**, 090705 (2014).
[25]G. Y. Fu, W. Park, H. R. Strauss, J. Breslau, J. Chen, S. Jardin, and L. E. Sugiyama, Phys. Plasmas **13**, 052517 (2006).
[26]J. A. Breslau, W. Park, and S. C. Jardin, J. Phys.: Conf. Ser. **46**, 97 (2006).
[27]N. Ferraro and S. Jardin, J. Comput. Phys. **228**, 7742 (2009).
[28]X. Ren, M. Chen, X. Chen, C. Domier, N. Ferraro, G. Kramer, N. Luhmann, Jr., C. Muscatello, R. Nazikian, L. Shi, B. Tobias, and E. Valeo, J. Instrum. **10**, P10036 (2015).
[29]O. Czarny and G. Huysmans, J. Comput. Phys. **227**, 7423 (2008).
[30]G. Huysmans, S. Pamela, M. Beurskens, M. Becoulet, and E. van der Plas, in Proceedings of the 23rd IAEA Fusion Energy Conference, Daejeon, South Korea (2010), pp. 11–16.
[31]S. Ku, R. Hager, C. Chang, J. Kwon, and S. Parker, J. Comput. Phys. **315**, 467 (2016).
[32]Y. Chen, J. Chowdhury, S. E. Parker, and W. Wan, Phys. Plasmas **22**, 042111 (2015).
[33]M. F. Adams, S.-H. Ku, P. Worley, E. D'Azevedo, J. C. Cummings, and C. Chang, J. Phys.: Conf. Ser. **180**, 012036 (2009).
[34]F. Zhang, R. Hager, S.-H. Ku, C.-S. Chang, S. C. Jardin, N. M. Ferraro, E. S. Seol, E. Yoon, and M. S. Shephard, Eng. Comput. **32**, 285 (2016).
[35]S. Balay, S. Abhyankar, M. F. Adams, J. Brown, P. Brune, K. Buschelman, L. Dalcin, V. Eijkhout, W. D. Gropp, D. Kaushik, M. G. Knepley, L. C. McInnes, K. Rupp, B. F. Smith, S. Zampini, H. Zhang, and H. Zhang, "PETSc web page," (Argonne National Laboratory, 2016).
[36]S. Balay, S. Abhyankar, M. F. Adams, J. Brown, P. Brune, K. Buschelman, L. Dalcin, V. Eijkhout, W. D. Gropp, D. Kaushik, M. G. Knepley, L. C. McInnes, K. Rupp, B. F. Smith, S. Zampini, H. Zhang, and H. Zhang, "PETSc users manual," Technical Report No. ANL-95/11-Revision 3.7 (Argonne National Laboratory, 2016).
[37]S. Balay, W. D. Gropp, L. C. McInnes, and B. F. Smith, in *Modern Software Tools in Scientific Computing*, edited by E. Arge, A. M. Bruaset, and H. P. Langtangen (Birkhäuser Press, 1997), pp. 163–202.
[38]H. Cai and G. Fu, Phys. Plasmas **19**, 072506 (2012).
[39]L. Guazzotto, R. Betti, J. Manickam, and S. Kaye, Phys. Plasmas (1994-present) **11**, 604 (2004).